

Mesh Adaptation for Improving Elasticity Reconstruction using the FEM Inverse Problem

Orcun Goksel, *Member, IEEE*, Hani Eskandari, *Member, IEEE*, and Septimiu E. Salcudean, *Fellow, IEEE*

Abstract—The finite element method is commonly used to model tissue deformation in order to solve for unknown parameters in the inverse problem of viscoelasticity. Typically, a (regular-grid) structured mesh is used since the internal geometry of the domain to be identified is not known a priori. In this work, the generation of problem-specific meshes is studied and such meshes are shown to significantly improve inverse-problem elastic parameter reconstruction. Improved meshes are generated from axial strain images, which provide an approximation to the underlying structure, using an optimization-based mesh adaptation approach. Such strain-based adapted meshes fit the underlying geometry even at coarse mesh resolutions, therefore improving the effective resolution of the reconstruction at a given mesh size/complexity. Elasticity reconstructions are then performed iteratively using the reflective trust-region method for optimizing the fit between estimated and observed displacements. This approach is studied for Young’s modulus reconstruction at various mesh resolutions through simulations, yielding 40% to 72% decrease in root-mean-square reconstruction error and 4 to 52 times improvement in contrast-to-noise ratio in simulations of a numerical phantom with a circular inclusion. A noise study indicates that conventional structured meshes with no noise perform considerably worse than the proposed adapted meshes with noise levels up to 20% of the compression amplitude. A phantom study and preliminary in-vivo results from a breast tumor case confirm the benefit of the proposed technique. Not only conventional axial strain images but also other elasticity approximations can be used to adapt meshes. This is demonstrated on images generated by combining axial strain and axial-shear strain, which enhances lateral image contrast in particular settings, consequently further improving mesh-adapted reconstructions.

Index Terms—Strain-based improvement of elastic parameter reconstruction, patient-specific modeling, trust-region method.

I. INTRODUCTION

CHANGES in tissue mechanical properties are known to be an indication of tissue anomalies. Therefore, the imaging of these properties, commonly referred to as *elastography*, can provide essential medical information for diagnosis and treatment planning. Since its introduction [1], [2], elastography has received significant attention from the research community, leading to various approaches proposed for the quantification

of shear modulus, such as measurement of the shear wave speed [3], [4], local frequency estimation [5], [6], the algebraic inversion of the Helmholtz equation [7], and several methods based on the acoustic radiation force [8]. See [9] for an extended summary of various methods. Elastographic techniques involve measuring tissue displacements in response to an excitation. Using these displacement measurements, the particular method then estimates one or more tissue mechanical parameters. The finite element method (FEM), a common tool for simulating continuum mechanics, is one of the methods used to derive mechanical characteristics from observed displacements.

In the context of FEM, modeling deformation for a given elasticity distribution over a domain is known as the forward problem (FP). Accordingly, reconstructing the viscoelastic properties of a medium from observed deformation is called the inverse problem (IP). The FEM provides a discretized *approximation* to the solution of a continuous deformation model; for instance, the wave equation discretized spatially over a *mesh* of simple geometric shapes, e.g. hexahedra. Consequently, the way in which the medium is discretized plays an important role in the accuracy of such approximation.

In the FEM FP of elasticity, the structure of the domain to be modeled is known or assumed *a priori*. Then, parameterized meshes that are fitted to the known shape of different regions are constructed. An example application is the deformable medical image registration, where a segmented anatomy is first meshed and then parameterized by assumed values from the biomechanics literature, in order to use to model anatomical deformations. In contrast in the IP, the internal structure of the domain is *not* known *a priori*. Then, often a *structured* mesh in the shape of a regular-grid is utilized to solve the IP in elastography, as well as in various other applications of the FEM IP. For FEM in general, there exist methods that subdivide or adapt the meshes iteratively to posterior FEM error estimates by using well-known mesh refinement techniques [10]. A similar approach has also been proposed in the context of elastography [11]. However, considering the IP, such posterior-error based methods require solving the computationally expensive IP multiple times. Also, a coarse mesh may lead to a suboptimal reconstruction yielding an inaccurate localization of where to subdivide for the next iterative reconstruction.

We have recently proposed a variational image meshing (*VIMesh*) method to automatically generate FEM meshes that are optimized to fit given input images [12]. Given the image representation of a domain in an arbitrary modality, this method optimizes the vertex positions and connectivity

Manuscript received June 13, 2012. This work was supported by the National Sciences Research and Engineering Council (NSERC) of Canada. *Asterisk indicates corresponding author.*

*O. Goksel is with the Computer Vision Lab of Swiss Federal Institute of Technology (ETH), Zürich, Switzerland (<http://people.ee.ethz.ch/~ogoksel/>).

H.Eskandari and S.E. Salcudean are with the Department of Electrical and Computer Engineering, The University of British Columbia, Vancouver, BC, Canada (email: {hanie,tims}@ece.ubc.ca).

of a mesh such that the image variation within each mesh element is minimized. With VIMesh, the underlying image is optimally discretized by the mesh. In this paper, this technique is adopted for elasticity reconstruction using the FEM IP and the generation of effective meshes is proposed using fast approximations to elasticity distribution. The use of strain images for this purpose is demonstrated.

The paper is organized as follows. First, the method used for elasticity reconstruction is detailed. Then, a brief summary of VIMesh is given. Next, the optimization approach and the effect of noise are studied comparatively. The results are demonstrated throughout the paper. They indicate significant improvement in elasticity reconstruction with the use of the proposed mesh adaptation scheme. A discussion and conclusions are provided at the end.

II. ELASTICITY RECONSTRUCTION

Elasticity reconstruction has been studied in the literature with quasi-static and harmonic excitations using the FEM IP by [13]–[19]. Please see [20] for a recent review. The elasticity reconstruction method presented in [13] is adopted in this work. For the purposes of this paper, damping is assumed to be small, thus the recovery of only the elastic parameter is presented. The method is summarized below for completeness; see [21] for a detailed derivation.

The deformation dynamics of a viscoelastic solid can be discretized by the FEM and written in time-domain as follows:

$$\mathbf{K}\mathbf{u}(t) + \mathbf{B}\dot{\mathbf{u}}(t) + \mathbf{M}\ddot{\mathbf{u}}(t) = \mathbf{f}(t) \quad (1)$$

where $\mathbf{K}, \mathbf{B}, \mathbf{M} \in \mathbb{R}^{3n \times 3n}$ are, respectively, the stiffness, the damping, and the mass matrices, and $\mathbf{u}, \mathbf{f} \in \mathbb{R}^{3n}$ are the vectors of nodal displacements and forces for an n -node discretization in 3D space.

For harmonic excitation, this can be written in frequency-domain by its Fourier transform as follows:

$$(\mathbf{K} + j\omega\mathbf{B} - \omega^2\mathbf{M}) \hat{\mathbf{u}} = \hat{\mathbf{f}} \quad (2)$$

where ω is the angular frequency of excitation and the hatted variables denote the Fourier transforms.

For small damping and a given density ($\approx 1 \text{ kg/m}^3$ for human soft tissue), this can be rewritten as follows:

$$(\mathbf{K}(\mathbf{p}) - \omega^2\mathbf{M}) \hat{\mathbf{u}} = \mathbf{A}(\mathbf{p}) \hat{\mathbf{u}} = \hat{\mathbf{f}} \quad (3)$$

where the stiffness matrix \mathbf{K} is a function of the elasticity parameter distribution \mathbf{p} and \mathbf{M} is constant. Finding the elastic parameters \mathbf{p} can be formulated as an optimization problem of finding $\hat{\mathbf{u}}$ that satisfies (3) and is *closest* (best-fit) to the displacement phasors $\hat{\mathbf{d}}$ measured at the angular frequency of excitation ω . In this paper, the Poisson's ratio is assumed to be known; thus, \mathbf{p} is the vector of Young's moduli for the mesh elements. Note that \mathbf{A} is a linear function of \mathbf{p} .

The forces $\hat{\mathbf{f}}$ along the discretization boundary are, in general, unknown non-zero quantities. In contrast, there exists no internal force inside the object, i.e. $\hat{\mathbf{f}}_\star = 0$ where the subscript \star denotes the vector components corresponding to internal mesh nodes. Similarly, the subscript \circ will be used throughout this paper to indicate the nodes on the domain

boundary. Without loss of generality, (3) can be rewritten in the following form:

$$\begin{bmatrix} \mathbf{A}_{\star\star} & \mathbf{A}_{\star\circ} \\ \mathbf{A}_{\circ\star} & \mathbf{A}_{\circ\circ} \end{bmatrix} \begin{bmatrix} \hat{\mathbf{u}}_\star \\ \hat{\mathbf{u}}_\circ \end{bmatrix} = \begin{bmatrix} \hat{\mathbf{f}}_\star \\ \hat{\mathbf{f}}_\circ \end{bmatrix} \quad (4)$$

$$\Rightarrow \begin{cases} \mathbf{A}_{\star\star}(\mathbf{p}) \hat{\mathbf{u}}_\star + \mathbf{A}_{\star\circ}(\mathbf{p}) \hat{\mathbf{u}}_\circ = \hat{\mathbf{f}}_\star & (5) \\ \mathbf{A}_{\circ\star}(\mathbf{p}) \hat{\mathbf{u}}_\star + \mathbf{A}_{\circ\circ}(\mathbf{p}) \hat{\mathbf{u}}_\circ = \hat{\mathbf{f}}_\circ & (6) \end{cases}$$

Applying the measured displacements $\hat{\mathbf{d}}_\circ$ along the boundary as a displacement boundary condition, i.e. $\hat{\mathbf{u}}_\circ = \hat{\mathbf{d}}_\circ$, and using the fact that $\hat{\mathbf{f}}_\star = 0$ for the internal nodes, (5) then becomes:

$$\mathbf{A}_{\star\star}(\mathbf{p}) \hat{\mathbf{u}}_\star = -\mathbf{A}_{\star\circ}(\mathbf{p}) \hat{\mathbf{d}}_\circ \quad (7)$$

where the right-hand-side represents the forces due to boundary displacements.

Finding the optimal parameters \mathbf{p}^* can then be formulated as an optimization problem for a least-square fit of the estimated displacements $\hat{\mathbf{u}}_\star(\mathbf{p})$, which is defined by (7) as a function of \mathbf{p} given $\hat{\mathbf{d}}_\circ$, to the observed displacements $\hat{\mathbf{d}}_\star$ at the internal nodes, as follows:

$$\mathbf{p}^* = \arg \min_{\mathbf{p} \geq 0} \left\| \hat{\mathbf{u}}_\star(\mathbf{p}) - \hat{\mathbf{d}}_\star \right\|^2 \quad (8)$$

In this paper, (8) is solved iteratively using the reflective trust-region method in Matlab[®] Optimization Toolbox. This is a two-dimensional subspace solver where the solution space is defined by the approximate Gauss-Newton direction found using preconditioned conjugate gradients. At each iteration given \mathbf{p} , we compute $\hat{\mathbf{u}}_\star$ using (7) and the Jacobian matrix $\mathbf{J} = \partial \hat{\mathbf{u}}_\star / \partial \mathbf{p}$ using the derivative of (7) as follows:

$$\frac{\partial \mathbf{A}_{\star\star}}{\partial \mathbf{p}} \hat{\mathbf{u}}_\star + \mathbf{A}_{\star\star} \frac{\partial \hat{\mathbf{u}}_\star}{\partial \mathbf{p}} = -\frac{\partial \mathbf{A}_{\star\circ}}{\partial \mathbf{p}} \hat{\mathbf{d}}_\circ \quad (9)$$

$$\Rightarrow \mathbf{A}_{\star\star}(\mathbf{p}) \mathbf{J} = -\frac{\partial \mathbf{A}_{\star\circ}}{\partial \mathbf{p}} \begin{bmatrix} \hat{\mathbf{u}}_\star \\ \hat{\mathbf{d}}_\circ \end{bmatrix} \quad (10)$$

where $\mathbf{A}_\star = [\mathbf{A}_{\star\star} \mathbf{A}_{\star\circ}]$. From (3), it is seen that $\partial \mathbf{A}_\star / \partial \mathbf{p} = \nabla_{\mathbf{p}} \mathbf{K}_\star$ is a sparse 3^{rd} -order tensor, which is constant for given mesh geometry and hence can be computed prior to the optimization. Below, we present our simulation framework.

III. SIMULATION SETUP AND PROBLEM DEFINITION

Simulations were carried out using two different 2D models with a square and a circular inclusion embedded in a $100 \times 100 \text{ mm}^2$ substrate as shown in Fig. 1(a). The fine FEM meshes seen in Fig. 1(b)-(c) are used to simulate the FP. The measured displacements are then used to reconstruct the elasticity parameters using different FEM IP tessellations (meshes). For evaluation, such reconstructions are compared to the original elasticity distributions in the FP.

Plane-stress was assumed and 6-node triangular elements with quadratic-interpolation functions, which provide better accuracy than linear elements, were used in both the FP simulations and the IP reconstructions. Both the square and the circular inclusion FP meshes have 1600 triangular elements and 3281 nodes including the mid-edge nodes. The Young's modulus of the inclusions and the substrates were set to 20 kPa and 10 kPa, respectively. Constant Poisson's ratio and density

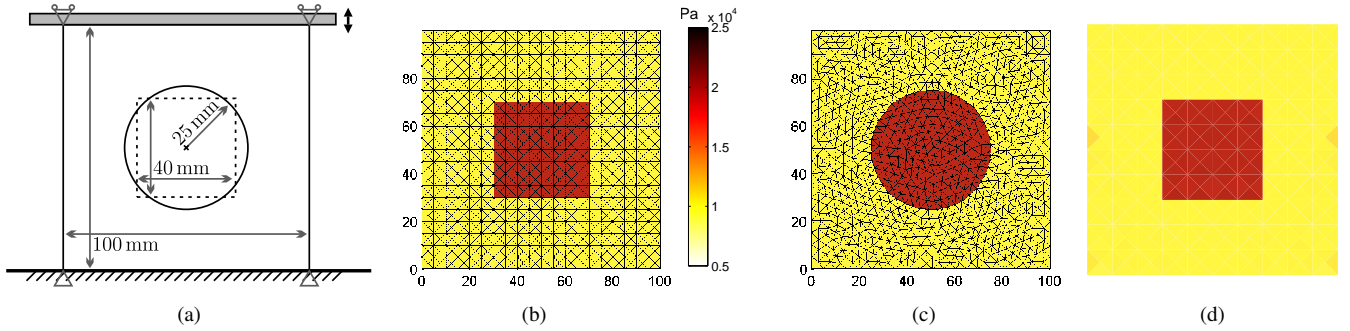


Fig. 1. (a) The models with square and circular inclusions used in the FP simulations; the FP FEM meshes of (b) the square and (c) the circular inclusion models; and (d) a reconstructed parameter distribution of the square inclusion. Note that FEM triangle mid-edge nodes are omitted from all the figures throughout the paper for clarity. The colorbar shown here is used in all the parameter reconstruction figures throughout this paper.

were set everywhere as 0.499 and 1000 kg/m^3 , respectively. The bottom sides of the meshes were fixed and the top edges were excited axially as shown in Fig. 1(a) with a 20 Hz harmonic sinusoid of 0.1 mm amplitude. Harmonic displacements at each FEM mesh node were then computed using (3).

Parameter reconstruction requires the displacement readings $\hat{\mathbf{d}}$ at the IP FEM mesh nodes. These were interpolated from the simulated FP model using element shape functions. Then, the methods of Sec. II were used to reconstruct the Young's modulus distribution. Fig. 1(d) shows a sample reconstruction of the square inclusion using a mesh with 400 elements and 841 nodes. This example exhibits a *nearly-perfect* elastic reconstruction. However, this success is biased by our deliberate choice of the mesh and square inclusion such that the mesh aligns perfectly with the inclusion boundary. In a general setting, one cannot know the location of an inclusion or any heterogeneity for that matter. Fig. 2 demonstrates parameter reconstructions of both inclusions at multiple mesh resolutions that do not necessarily coincide with the inclusion. In this figure and throughout the rest of this paper, the IP meshes are numbered from #4 to #12 based on the number of triangles spanning a side of a mesh. As seen (and also quantitatively presented later in Sec. VI), the non-compliant meshes perform suboptimally compared to the above inclusion-compliant case.

In general, higher mesh resolutions are preferred in FEM literature for better estimation of complex or high-strain deformations, and accordingly various mesh refinement methodologies exist [10]. Nonetheless, the suboptimality in the above-presented reconstructions arises due to suboptimal mesh discretization with respect to the location of inhomogeneity that was aimed to be captured. As each FEM element is assigned with the parameters of one particular material, the alignment of such elements with the internal geometry of the medium may thus cause element discretization errors with respect to spatial parameter distribution. Eliminating this error in FP FEM analysis, where the material boundaries are known *a priori*, is only a matter of meshing the volume with boundary compliant elements so no element will occupy two different materials. However, in the IP case in which the underlying property distribution is what needs to be reconstructed by the FEM and is unknown initially, such a mesh cannot be chosen/constructed *a priori* and often a regular-grid mesh is then used in the literature. At arbitrarily high mesh resolutions

such discretization errors become minute. However, due to computational constraints such as memory and computation time, large-scale physical problems and realtime applications are often solvable only using relatively coarse meshes.

As presented in this paper, customized coarse meshes can indeed generate comparable or even better elasticity reconstructions. For instance, note meshes #10 and #12 on row 2 of Fig. 2. Even though the former is coarser, it provides a better reconstruction due to our deliberate choice of its inclusion-compliant mesh in order to demonstrate this problem and motivate our solution. We propose *customized* coarse meshes for achieving better parameter reconstructions than those that can be obtained by using traditional structured meshes. Such coarse meshes become increasingly important for large-scale physical problems and realtime applications, e.g. the tissue elasticity reconstruction, for which finer IP meshes are impracticable due to computational limitations such as storage and runtime. In order to better demonstrate our motivation, the next section illustrates FEM approximation with respect to element placement on a simplified 1D elasticity example.

IV. PROBLEM MOTIVATION ON A 1D EXAMPLE

The IP estimates the elasticity value of every element in a model using nodal displacements. In the typical form of the FEM formulation, a constant elasticity is considered within each element. Similarly, the IP also solves for a *single* elasticity value for each element, even though the physical continuum being modeled may exhibit arbitrary variation within such element. Consider the 1D example in Fig. 3(a) where the displacements in a medium with two separate regions of unknown stiffnesses are observed. Assume that, in order to recover the underlying (unknown) stiffness distribution, a model with 3 equidistant elements is used by acquiring the noise-free displacement readings at the circled 4 nodes. It is evident that this 1D mesh is unable to estimate the continuum elasticity distribution within the middle element, due to the way in which the domain is discretized. Even using higher order element interpolations cannot capture the stiffness variation within the center element. Note that in this case, a simpler model with only 2 elements with its mid-node at the interface of the two regions theoretically yields a perfect reconstruction even using simple linear basis functions. In fact, this is also the best approximation achievable for this toy problem; even

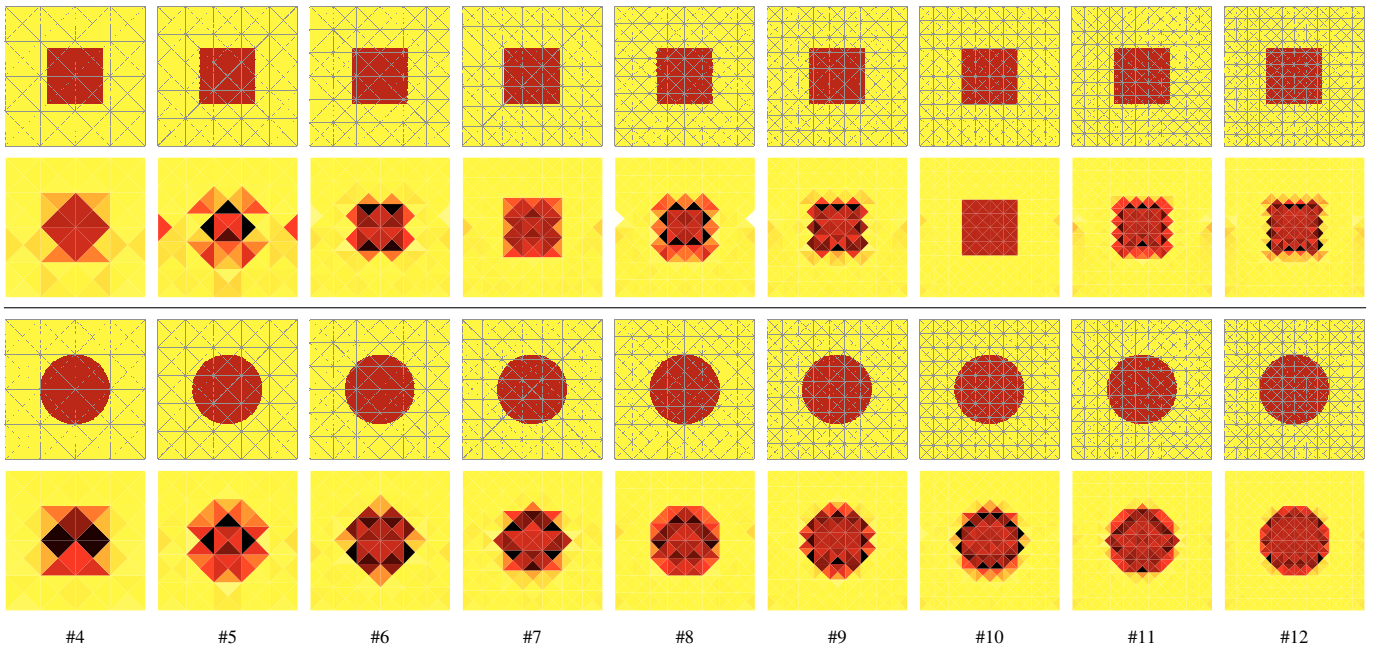


Fig. 2. IP parameter reconstruction of the square (top) and the circular (bottom) inclusions using structured triangular meshes. The mesh number indicate the number of triangles along the mesh edge; e.g. mesh #4 having 64 triangles is the coarsest mesh shown here and #12 is the finest with 576 triangles. The first and the third rows show the meshes overlaid on the ground-truth inclusion as a reference. The second and the fourth rows show the reconstructed parameter values for each element using the range of the colorbar as given above in Fig. 1 with the values outside this range clipped (the parameter reconstruction considers a much wider Young’s modulus range: 0–100 kPa).

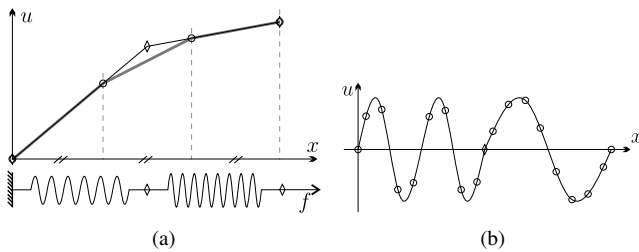


Fig. 3. (a) A sub-optimal reconstruction of 1D stiffness distribution from a quasi-static compression using three equi-length (non-domain-compliant) elements. A perfect reconstruction is possible if and only if an element border aligns with the (unknown) interface of different stiffnesses. (b) A similar example for a dynamic case, where sample aliasing at the interface may cause complications, e.g. higher order harmonics, depending on the choice of reconstruction method.

compared to several higher mesh resolutions that do not align with the region boundary, e.g. a 101-segment model with its mid-element still having some (though small) discretization error. Our goal then is to generate optimal discretizations for domains, the elasticity distributions of which are not known *a priori*. To that end, we propose to use fast imaging modalities such as strain imaging to approximate such distribution and adjust a mesh prior to solving the FEM IP. Note that typical methods of mesh refinement (e.g., higher strain elements [10]) will not refine that mid-element, and thus do not provide a solution to this problem.

Under dynamic excitation as seen in Fig. 3(b), mesh compliance to underlying stiffness and boundary interfaces may similarly cause complications during reconstruction, such as parameter over- or under-estimations near such regions, depending on the methods chosen for estimation of phasors $\hat{\mathbf{d}}$

and for reconstruction of \mathbf{p}^* in (8). These can also be observed in our simulations in Fig. 2, in which values outside the 10–20 kPa range are observed.

The simple 1D example above is presented merely to motivate the problem of optimal element placement, the solution of which in 1D is relatively straight-forward. However, a general method in higher spatial dimensions for arbitrary underlying distributions is not obvious. The next section describes our mesh adaptation approach that reduces the aforementioned discretization artifacts and enables the use of coarser meshes without compromising spatial reconstruction precision.

V. MESH ADAPTATION USING VIMESH

Let $h(\mathbf{x})$ represent the intensity of a given image at spatial location \mathbf{x} and \mathbf{x}_i denote the vertices of an FEM model that is used to discretize the domain covered by this image. In order to find an optimum tiling of an image, a cost function is proposed in [12] as the image intensity variance within each FEM element. This cost is given formally as follows:

$$\mathbb{E}_D(\{\mathbf{x}_i\}, \{\tau_i\}, h) = \sum_i v_i \text{var}(h(\mathbf{x}) | \mathbf{x} \in \tau_i) \quad (11)$$

where v_i is the volume of element i , τ_i is the tetrahedron representing this element, and var is the second moment of intensity distribution about its mean, that is the intensity variance within the element. Here, $\{\cdot\}$ denotes sets, e.g. the set of all vertices or tetrahedra in a mesh. Note that \mathbb{E}_D is the squared difference (\mathcal{L}^2 -norm error) between the image intensities $h(\mathbf{x})$ and their local mean value \hat{h}_i within each element τ_i . Given an image, minimizing this error over all possible FEM discretizations then finds the optimal mesh: the vertex positions $\{\mathbf{x}_i\}$ and their tessellation $\{\tau_i\}$.

FEM simulation performance pertains closely to element shapes. For instance, it is known that *slivers* (flat tetrahedra with all four vertices lying near the equator of a sphere) cause inaccurate results and numerical instabilities [22]. In 2D, skinny triangles have a similar defect. Aspect ratios and other measures were introduced to detect such degeneracies [22], [23] and various mesh smoothing strategies have been proposed in the literature in order to obtain high-quality elements [24], [25]. Similarly, a mesh penalty is defined in our mesh adaptation scheme in order to avoid degenerate cases. It is based on the Optimal Delaunay Triangulation (ODT) smoothing strategy [26], [27] and is given as follows:

$$\mathbb{E}_G(\{\mathbf{x}_i\}, \{\tau_i\}) = \frac{1}{N+1} \sum_i \mathbf{x}_i^2 |\Omega_i| - \int_{\mathcal{M}} \mathbf{x}^2 d\mathbf{x} \quad (12)$$

where Ω_i is the *1-ring neighbourhood* of node \mathbf{x}_i , that is the set of elements having \mathbf{x}_i as a corner. Intuitively, (12) is the difference (error) between a quadratic function \mathbf{x}^2 and its piece-wise linear approximation over a tessellation. $|\Omega_i|$ is the aggregate area/volume of the elements neighbouring node i . Then, the first term in (12) is the numerical integration of the quadratic function using the trapezoidal rule. Note that the integral term in (12) is constant and thus can be precomputed for a given domain size/shape \mathcal{M} . Minimizing \mathbb{E}_G effectively results in a smooth distribution of nodes providing theoretical guarantees on certain mesh qualities. More on ODT can be found in [26].

A weighted average of (11) and (12) is then minimized [12] using Lloyd's relaxation scheme, where vertices and elements are updated iteratively yielding the optimal mesh as follows:

$$(\mathbf{x}^*, \tau^*) = \arg \min [(1 - \lambda)\mathbb{E}_G + \lambda\mathbb{E}_D] \quad (13)$$

where $\lambda \in [0, 1)$ is the weighting factor. This technique, VIMesh, was demonstrated on MR and CT images in 2D and 3D in [12] with quantitative comparisons to other meshing tools common in the field of medical imaging and it was shown to yield effective FEM meshes. In elasticity reconstruction, \mathbb{E}_D can be thought to penalize elements crossing object interfaces and extending between regions with different elasticity values, and \mathbb{E}_G to ensure mesh suitability for the FEM.

Motivated by the ease of obtaining axial strain images in ultrasound, we use them for mesh adaptation. For simulations, strain images of the two aforementioned synthetic models were generated using quasi-static axial compression in the FEM FP. The simulated displacements were then interpolated on a 200x200 regular-grid with the axial gradient yielding the strain images shown in Fig. 4(a)-(b). The mesh adaptation procedure is exemplified for the case of a circular inclusion in Fig. 4. The final optimized mesh is then used for parameter reconstruction as in Sec. II.

In general, the elasticity distribution cannot be reconstructed exactly from strain images due to boundary condition effects. Nevertheless, contrast at elasticity change can still drive the mesh to adapt to such regions, which in turn enhances the effective spatial resolution of the IP reconstruction. In Fig. 5, meshes adapted to the strain images of a square and a circular inclusion are shown along with parameter reconstructions using such adapted meshes, demonstrating significant improve-

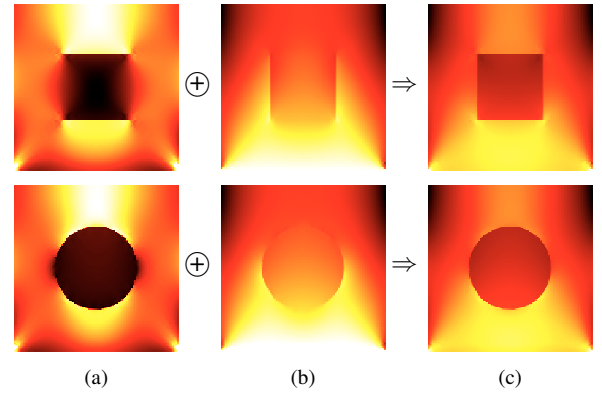


Fig. 6. Images of (a) axial strain, (b) axial-shear strain, and (c) their combination, for the square (top) and the circular (bottom) inclusion phantoms, respectively. Each strain image is normalized within itself and intensity-wise summed up for the purposes of this simple example, where the intent was to preserve inclusion boundary contrast from both modalities.

ment compared to structured meshes presented earlier in Fig. 2. Improvement in reconstructions is demonstrated quantitatively later in Sec. VI.

The proposed mesh adaptation scheme is not limited to axial strain images alone, but can also be applied using other elasticity approximations to adapt meshes. To demonstrate this, axial-shear strain images of the same models are employed. These were synthetically obtained by a 0.1 mm lateral quasi-static excitation of the phantom surface while still observing the axial displacements. As seen Fig. 6(a)&(b), the lateral inclusion boundaries are sharper in these images in contrast to axial strain images for this given configuration. In order to incorporate contrast from both axes, these two modalities are then combined as seen in Fig. 6. For the purposes of this example, a simple summation of normalized intensities from each modality is performed. Subsequently, mesh adaptation is applied to these combined images. The resulting parameter reconstructions are given in Fig. 7, demonstrating both the feasibility of using other imaging methods for mesh adaptation and the potential for improving upon the axial-strain adapted results in certain scenarios.

VI. QUANTITATIVE EVALUATION

For the evaluation of elasticity reconstructions, the root mean square error (RMSE) and the elastographic contrast-to-noise ratio (CNR) are used [28]. Let p_i be the parameter estimated for element τ_i using the IP. The RMSE is the parameter reconstruction error typically defined *element-wise* in the literature, i.e. the difference between the known FP and the reconstructed IP element values. However, as the element sizes/placements differ between FP and IP in our case, we resort to a discrete definition by numerical integration as follows:

$$\text{RMSE} \stackrel{\text{def}}{=} \sqrt{\frac{1}{|V|} \int_V \frac{|p(x) - p^0(x)|^2}{|p^0(x)|^2} dx} \quad (14)$$

$$\approx \sqrt{\frac{1}{m} \sum_{k=1}^m \frac{|p[k] - p^0[k]|^2}{|p^0[k]|^2}} \quad (15)$$

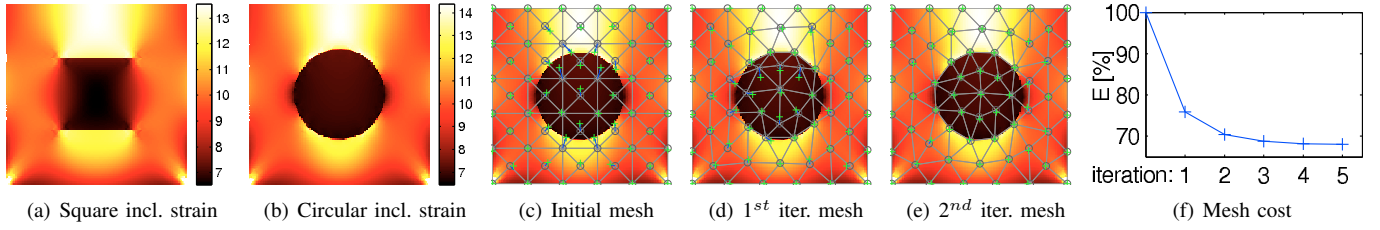


Fig. 4. Axial strain images of (a) the square and (b) the circular inclusion models; (c) the strain image of the circular inclusion, overlaid with a 100-element structured mesh, that was used to initialize mesh adaptation; (d)-(e) mesh configurations after the first and the second iterations; and (f) the convergence of the objective function (13) during this adaptation procedure.

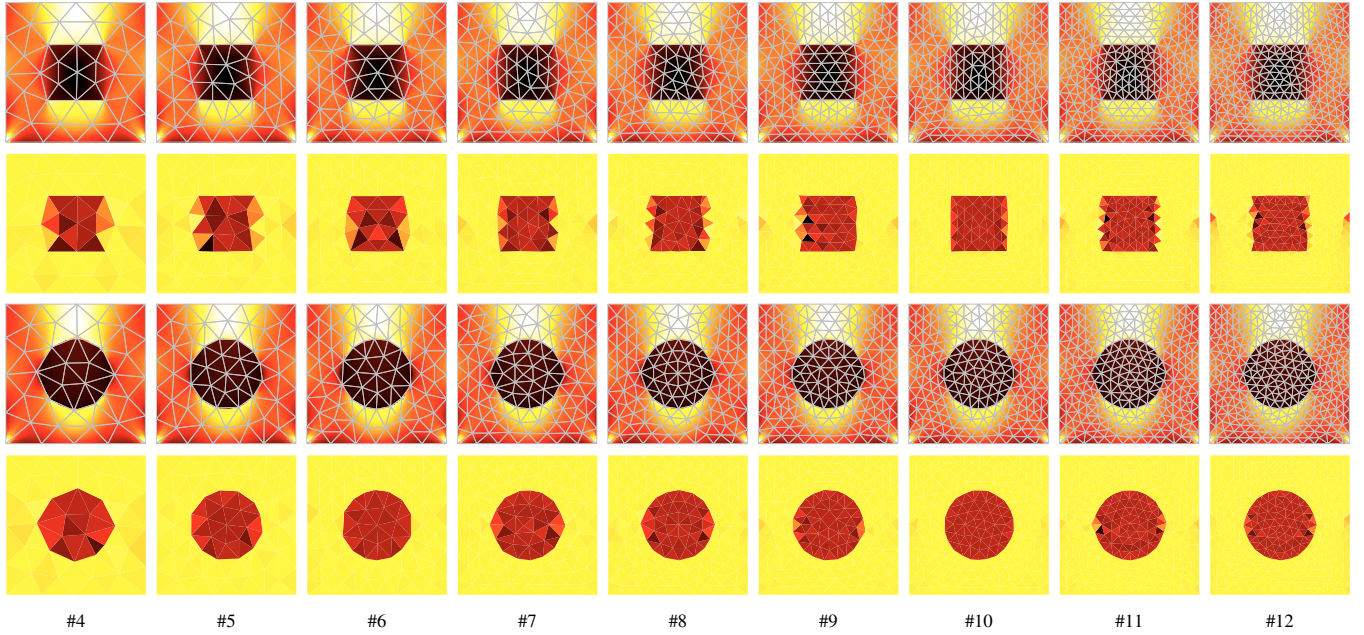


Fig. 5. Meshes fitted to axial strain images and improved parameter reconstruction results obtained using such meshes. In this paper, a fixed number of 5 iterations are carried out for each mesh adaptation example presented.

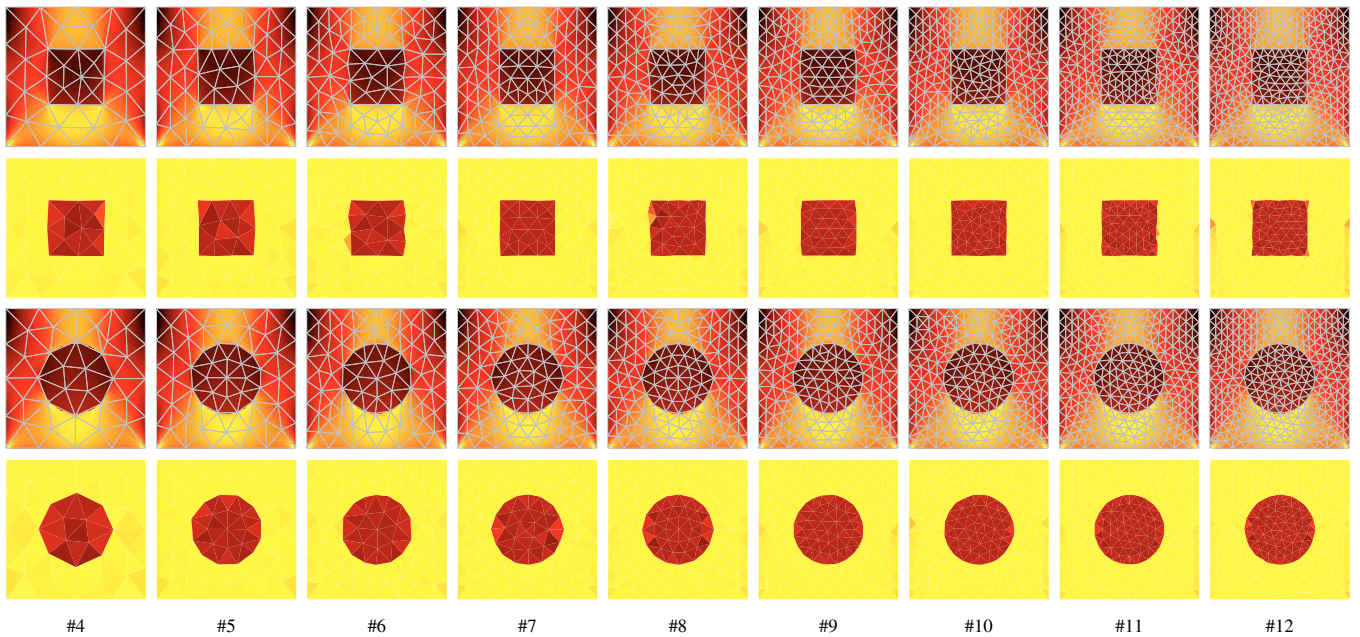


Fig. 7. Mesh adaptation to the *combined* axial and axial-shear strain images seen in Fig. 6 and the resulting parameter reconstructions.

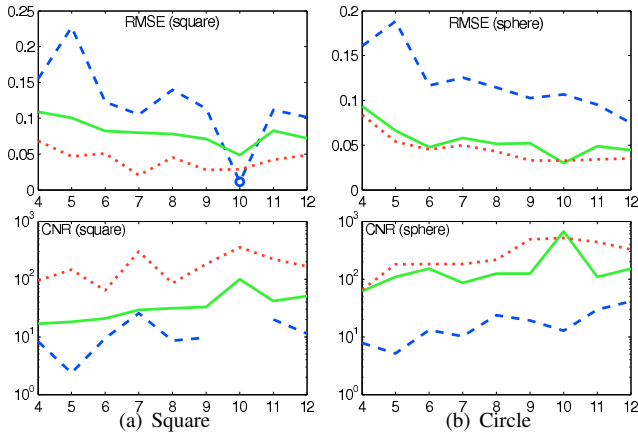


Fig. 8. Quantitative assessment of reconstruction performance using RMSE (top) and CNR (bottom) metrics for the square (a) and the circular (b) inclusions. The results are shown with dashed lines (--) for the structured meshes in Fig. 2, with solid lines (—) for the axial-strain adapted meshes in Fig. 5, and with dotted lines (· · ·) for the combined-strain adapted meshes in Fig. 7. The x -axes denote the mesh number. The structured square mesh #10 marked with an * is by definition a “perfect” match to the inclusion and thus generates an artificial contrast (with CNR greater than 8×10^3). This data-point is therefore excluded from the corresponding CNR figure.

where p^0 is the known ground-truth and p is the reconstructed parameter value at a point x , and m is the number of integration points. The value $p[k]$ of an integration point k is the value p_i of the mesh element τ_i that encloses k , i.e.:

$$p[k] = p_i \quad \text{where} \quad x[k] \in \tau_i \quad . \quad (16)$$

The ground-truth values $p^0[k]$ are referred from the FP mesh, whereas the reconstructed values $p[k]$ are from the IP mesh.

CNR is used as a measure of inclusion contrast in a reconstruction and it is defined as [28]:

$$\text{CNR} \stackrel{\text{def}}{=} \frac{2(e_{\text{inc}} - e_{\text{bkg}})^2}{\sigma_{\text{inc}}^2 + \sigma_{\text{bkg}}^2} \quad (17)$$

where e is the average mean and σ is the standard deviation of the reconstructed elasticity parameters $p[k]$ inside (inc) and outside (bkg) a known inclusion, i.e. $e_{\text{inc}} = \text{mean}(p[k] | x[k] \in \text{inc})$. Note that CNR pertains only to reconstruction and does not depend on ground-truth distribution.

RMSE and CNR comparisons of the parameter reconstructions using the conventional structured and the proposed adapted meshes are presented in Fig. 8. Note the substantial improvement in RMSE, which correlates with the earlier qualitative observations from the reconstruction figures.

VII. ANALYSIS OF NOISE ON SYNTHETIC DATA

Various sources of noise can affect reconstructions in a practical setup of the presented system. Noise in displacement measurements may cause both sub-optimal mesh fitting and incorrect parameter estimation. In this section, we study the effect of noise on the measured displacement phasors $\hat{\mathbf{d}}$ using numerical simulations. The origin of such noise in practice can be the image acquisition setup, the displacement estimation technique, the phasor estimation step, or a combination thereof. For simulations, after having adapted meshes and having interpolated displacement observations at the IP mesh

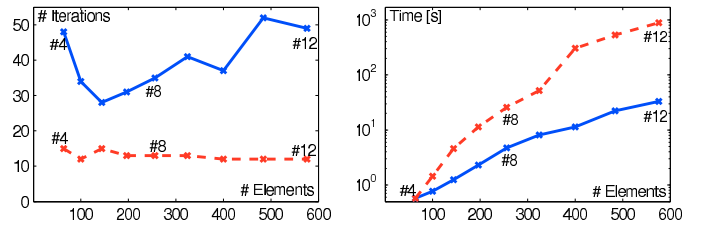


Fig. 11. Iterations (left) and time (right) required for the Levenberg-Marquardt (dashed line) and the reflective trust-region (solid line) optimization methods for different mesh resolutions. The number of elements are shown in the x -axis with simulation mesh numbers marked. Note that a mesh with our numbering $\#k$ includes $4k^2$ triangular elements and $8k^2 + 4k + 1$ nodes.

nodes from the FEM FP, a uniform random noise is added to the displacement phasor amplitudes following mesh adaptation but prior to the solution of the IP.

Reconstruction RMSE and CNR are given for three different mesh resolutions in Fig. 9, in which the simulated noise amplitude was varied up to 30% of the compression amplitude. Noise simulations were repeated on both the structured and the axial-strain adapted meshes. At all noise levels, both RMSE and CNR indicate better reconstruction results with adapted meshes compared to their structured counterparts. Fig. 10 presents some sample reconstructions with noisy data.

VIII. OPTIMIZATION

The Levenberg-Marquardt (LM) optimization method is commonly used in the literature to solve the inverse problem of elasticity [13], [14], [21]. Although LM can approach the solution much faster at each iteration for a carefully chosen Marquardt parameter (weighting between Gauss-Newton and steepest descent directions [14]), adjusting such regularization at each iteration is non-trivial. In this work, we employed a reflective trust-region (TR) method due to several reasons. This method allows for lower/upper parameter bounds to be imposed as optimization constraints. It also does not require the construction of a Hessian matrix, reducing storage and computational complexity, and hence scaling better with increasing mesh size. In Fig. 11, the number of iterations and the total time taken by Matlab[®] implementations of these two optimization methods are compared for IP reconstruction on different sizes of our adapted meshes to the circular inclusion (Fig. 5, row 3). Even though the trust-region method requires a larger number of iterations, its faster evaluation achieves convergence in less total time, in particular for larger meshes; e.g. for mesh #12, LM takes 15 min whereas TR completes in 30s. Therefore, TR was our choice of optimization in this paper. The RMSE and residual progress of these two approaches are also presented in Fig. 12 for mesh #8. Solution snapshots taken at selected iterations are illustrated in Fig. 13 to remark the different solution ‘paths’ taken by these two different algorithms in the parameter space.

IX. EXPERIMENTS

Experiments have been performed using a setup similar to the one described in [29]. First, cross-section of a breast biopsy phantom (CIRS Inc., Norfolk, VA) was imaged using

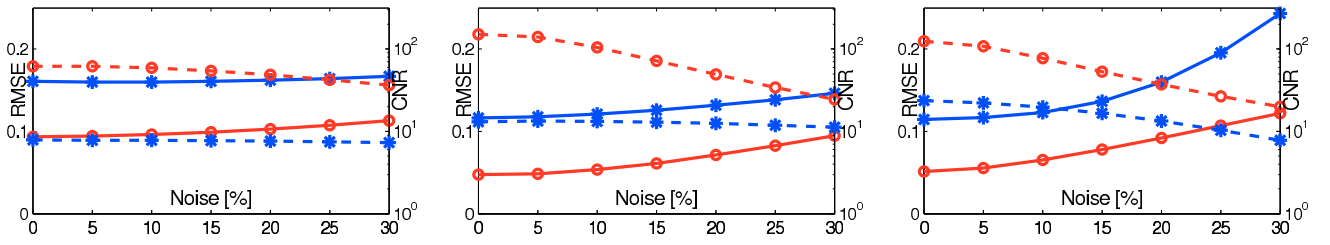


Fig. 9. Parameter reconstruction results for meshes #4 (left), #6 (center), and #8 (right) with structured (marked with *) and adapted (marked with o) meshes under displacement noise. The solid lines (—) show RMSE with axes on the left, and the dashed lines (---) show CNR with axes on the right of each figure. The x -axes show the simulated noise magnitude normalized to the compression amplitude.

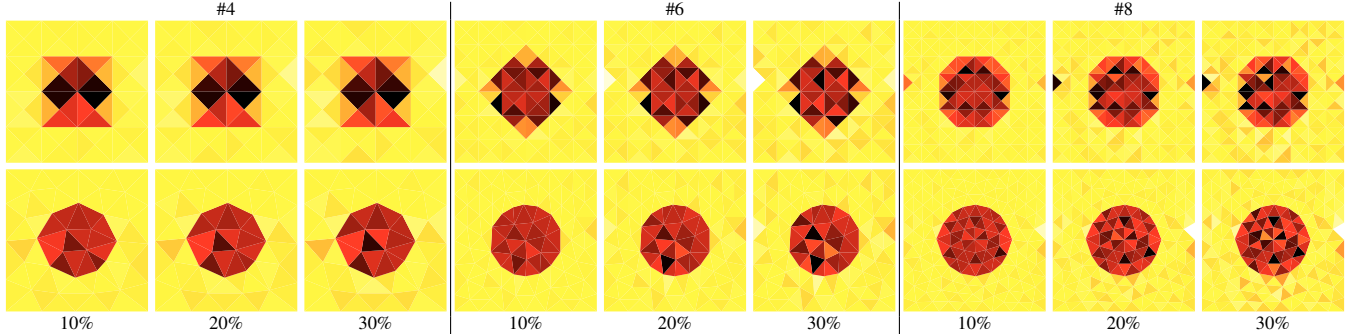


Fig. 10. Some reconstruction results from Fig.9 with the top and bottom rows showing structured and adapted meshes, respectively.

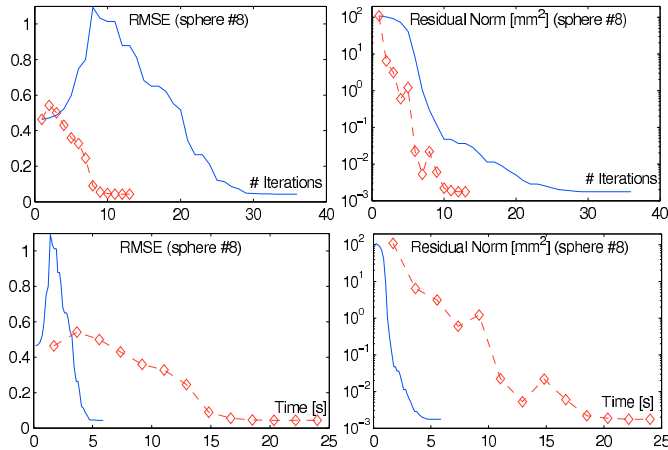


Fig. 12. RMSE (left) and residual (right) comparisons between the Levenberg-Marquardt (LM) (dashed line) and the reflective trust-region (solid line) optimization methods during the parameter reconstruction of 8×8 mesh adapted to the circular inclusion (#8 in Fig. 5 lower row). Results are presented in iterations (top) and in time spent (bottom). LM function evaluations are marked by \diamond . Our LM implementation for this example omits line-search as this worked more effectively than the internal Matlab implementation with line-search.

Then, the Marquardt parameter is simply reduced by an order of magnitude after each function evaluation that decreases the residual. Non-decreasing evaluations are the reason for the seldom residual increases.

a SonixTouch ultrasound system (Ultrasonix Medical Corp., Richmond, BC) at a frame rate of 104 Hz. The ultrasound center frequency was 10 MHz and the signal was sampled at 40 MHz. Using a linear-array transducer, 64 RF-lines along the 38 mm lateral transducer span were collected up to a depth of 40 mm. Harmonic vibrations were applied to

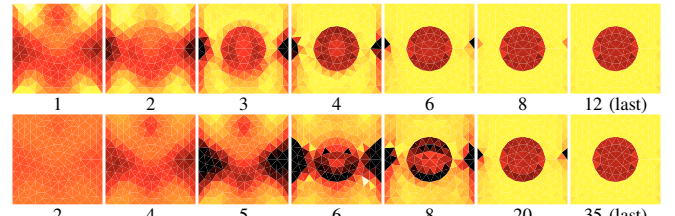


Fig. 13. IP reconstructions at selected iterations of the Levenberg-Marquardt (top row) and the reflective trust-region (bottom row) optimization methods.

the phantom using a voice-coil actuator. The displacements were tracked in the RF data between each consecutive pairs of acquired ultrasound frames using a time-domain cross-correlation method that uses displacement priors obtained from neighbouring estimation results [30]. Each 2080-sample RF line was divided into 100 blocks with 50% overlap and axial displacements were estimated by finding the peaks of the cross-correlation functions. The displacement phasor \hat{d} of each block is then obtained using the Fourier-transform of the displacement estimate of that block over time. This configuration yields a spatial data resolution of 0.4 mm axially and 0.6 mm laterally. Results below were computed within a centered region of interest to avoid displacement estimation and boundary condition artifacts near image borders.

A vibro-elastography image seen in Fig. 14(a) was reconstructed at 15 Hz excitation [21]. This is practically a strain image as, at low frequency, vibro-elastography is an acquisition and processing technique for robustly estimating the strain map in the tissue [31]. This image is then used to adapt meshes with different resolutions. Young's modulus reconstructions

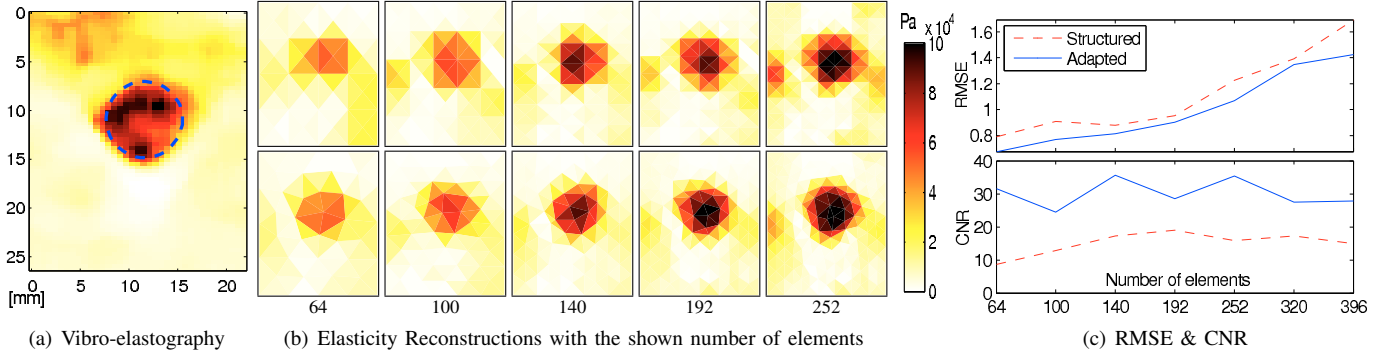


Fig. 14. Experimental results on tissue-mimicking phantom. (a) A vibro-elastography image; (b) reconstructions using structured (top) and adapted (bottom) meshes. (c) RMSE and CNR metrics for seven mesh resolutions (only five coarser ones are plotted due to space considerations). The metrics were computed with an assumed inclusion location marked in (a). The number of FEM nodes in these meshes, respectively, are [145, 221, 305, 413, 537, 677, 833].

are then performed at a frequency of 65 Hz from observed axial displacement data, by modifying the objective function in (8) using the internal axial displacements alone. On the boundary, the measured axial displacements are applied as the constraint and the lateral displacements are assumed to be zero. The reconstructions using different resolutions of structured and adapted meshes are seen in Fig. 14(b).

For a quantitative assessment, the approximate inclusion location is delineated in Fig. 14(a) and used to compute reconstruction CNR reported. We have also computed RMSE estimates for the reconstructions. To that end, although precise elasticity values in this phantom were not reported, the phantom substrate have been estimated to be 12 kPa experimentally from the spatial wavelength. The embedded inclusion being roughly five times stiffer is then 60 kPa. The results are given in Fig. 14(c), which indicates improvement in reconstructions by using mesh adaptation.

The same acquisition setup was used for an in-vivo study of breast cancer, the preliminary results of which are shown in Fig. 15. A tumor is seen in the B-mode and vibro-elastography images on the left. Next, elasticity reconstructions of this region at two different mesh resolutions repeated with structured and strain-adapted meshes are presented. Note that these are the direct reconstruction results without any post-processing.

X. DISCUSSION

The RMSE and CNR results previously plotted in Figs. 8 are tabulated here in Table I in order to summarize the improvement achieved by using mesh adaptation. In these tables, the circular inclusion example is presented for being a better representation of the typical pathological geometry with mesh adaptation to simple axial strain images, as this imaging modality is readily available in many applications. Table I suggests an RMSE improvement of 42% to 72% and a CNR improvement of 4 to 52 times in these simulations.

Even at relatively high noise levels, the proposed method provided improved reconstructions. Indeed, in all three examples in Fig. 9, the RMSE with 20% noise after mesh adaptation is observed to be less than that of structured meshes that are noise-free. This leads to the following remarkable conclusion

TABLE I
TABULATION OF RMSE AND CNR IN FIG. 8(B) FOR COMPARISONS BETWEEN RECONSTRUCTIONS USING STRUCTURED MESHES AND THE MESHES ADAPTED TO THE CIRCULAR INCLUSION AXIAL STRAIN. THE IMPROVEMENT IN ERROR AND CONTRAST ARE GIVEN, RESPECTIVELY, IN PERCENTAGE [%] AND AS A RATIO [×].

Mesh number	RMSE		improvement [%]	Mesh number	CNR		improvement [×]
	structured	adapted			structured	adapted	
#4	0.161	0.093	42.0	#4	7.8	61.8	7.9
#5	0.188	0.066	65.0	#5	5.2	108.7	21.0
#6	0.117	0.048	59.2	#6	13.1	151.7	11.6
#7	0.125	0.058	53.6	#7	10.1	85.6	8.4
#8	0.114	0.051	55.1	#8	23.6	124.2	5.3
#9	0.103	0.052	49.2	#9	19.2	125.0	6.5
#10	0.107	0.030	71.9	#10	12.8	672.9	52.4
#11	0.095	0.049	48.9	#11	29.4	108.9	3.7
#12	0.075	0.044	40.4	#12	41.2	151.8	3.7

that using a sub-optimal mesh in that given scenario introduces a reconstruction inaccuracy similar to having a measurement noise of more than 20% of the compression amplitude.

Although strain images may contain strain artifacts and these may affect the meshing generating element/node placement accordingly, the final reconstructed parameters will not contain such artifacts since the following IP elasticity reconstruction step resolves the actual parameter values for all elements regardless of their tessellation. While the elements capturing the details improve reconstruction precision, the ones adapting to artifacts are simply resolved by the IP. This can be observed in Fig. 5 where the apparent relative softening (high strain) above the inclusion is *not* translated to the reconstruction images.

FEM discretization may induce errors due to both displacement approximation and spatial viscoelastic-property distribution approximation. In simulations with the perfectly inclusion-compliant mesh (Fig. 1(d)), the latter error is eliminated whereas the former still prevails. In Fig. 2 (row 2, #10), this case is compared with both finer and coarser meshes, for which displacement errors are smaller and larger, respectively. As seen, in both cases the reconstructions are worse, except when the mesh fits the inclusion (#10) thereby removing the property distribution errors. A square inclusion can have an intrinsically compliant structured mesh, facilitating the demonstration of our problem motivation. Mesh adaptation has been

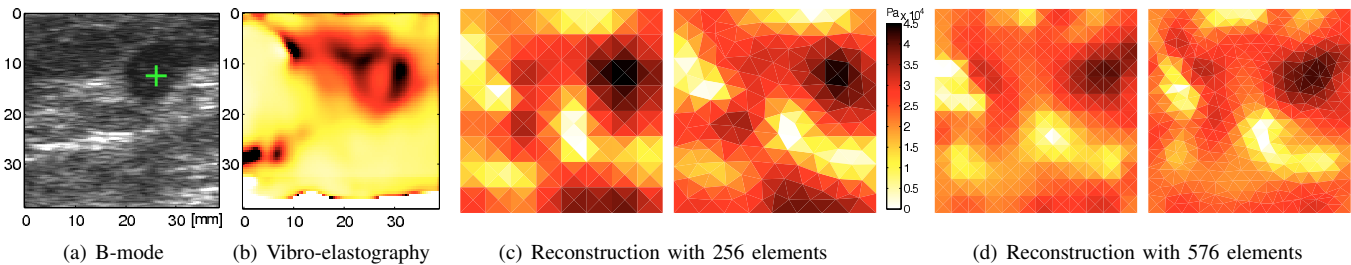


Fig. 15. B-mode and vibro-elastography images of a breast tumor (marked with +) and its elasticity reconstructions with structured and adapted meshes.

proposed as a general solution for arbitrary inclusion geometry. The last row in Fig. 5 shows that adapted meshes at several *different* resolutions result in relatively similar (successful) reconstructions, whereas the displacement discretization errors will naturally vary across those resolutions. Accordingly, our results show that *even in the existence of displacement discretization errors*, viscoelastic parameters are reconstructed better, *once the property-distribution discretization errors are minimized*.

The elasticity inverse problem in general is ill-posed. In the literature [32], [33], image segmentation was proposed to generate spatial priors for intravascular elastography in order to overcome this ill-posed nature by restricting the solution domain. It involves an expert delineating the regions that are believed to contain tissues with different elastic modulus, and then the reconstruction being performed by solving only a small system with few viscoelastic parameters representing each such identified region. In contrast, our method solves a system of parameters with the same degrees of freedom as that of the same-sized structured mesh. The spatial priors technique targets offline computation as an expert has to intervene for segmentation. Furthermore, it assumes that all modulus interfaces are identifiable in the medical image itself. Its goal then is to determine the modulus value, not the unknown location of an inclusion. In contrast, the general problem of elastography aims to both locate and parameterize a section of tissue, e.g. a tumor. Such tissue regions in general are not necessarily resolvable in other medical imaging modalities. Even if they are identifiable and elastography is merely performed to parameterize elasticity, still the delineation of a spatial prior is not practicable in a realtime online setting such as ultrasound elastography, which is the focus of our work.

The synthetic simulations were designed to demonstrate that parameter reconstruction errors may originate from suboptimal element discretization. A more complete simulation system would have included ultrasound image simulation (such as RF generation using Field II) and subsequent motion estimation. However, such a simulation would have added other sources of image degradation which would then make it difficult to identify and to present the origin of any reconstruction errors.

In our experimental setup, the boundary condition assumptions and a spatial smoothing of Young's modulus between elements were sufficient to generate stable results. To study the effect of meshing alone in the simulations, we assumed the lateral displacements to be present. In practice, lateral observations are available in MR elastography or are possible

to obtain using methods such as [34], [35] in ultrasound elastography. For magnetic resonance images, for which all displacement directions are available, it is worth investigating the octahedral shear strain (OSS, [36]) method for generating images for mesh adaptation.

We have used 6-node triangular elements with quadratic interpolation functions in the IP. Following structured or adaptive meshing with 3-node triangles, mid-edge nodes were added yielding the 6-node quadratic elements. These offer certain advantages compared to linear elements. For instance, in cases where the number of constraints (measured displacements: nodes \times axes) are not sufficient for a unique solution, additional assumptions are required, such as known/assumed values for some elements [37]. In contrast, 6-node elements by definition introduce a larger number of equations (per node) in the system than the unknowns (per element) to be solved. Therefore, even in the case of axial displacements alone, no assumptions are needed other than some practical bounds for the parameters being optimized. Furthermore, we observed such 6-node quadratic elements to also improve the IP reconstruction significantly in comparison to linear triangles, which often led to unstable reconstructions. This can be due to locking of linear triangular elements. Another likely contributing factor is that quadratic interpolation functions can approximate the locally sinusoid-like spatial variation (pattern) of steady-state harmonic waves more accurately than linear interpolation functions.

Mesh adaptation to combined strain images has been presented in order to demonstrate that: (i) our mesh adaptation is applicable to a wider range of applications and imaging modalities in the field of elastography, and (ii) the input image contrast can be improved beyond what axial strain images can offer alone. The former was also supported by the presented experiment that exemplifies the use of vibro-elastography images for mesh adaptation. The latter was shown by improving axial strain images using axial-shear strain, which can provide contrast at lateral interfaces. Reconstructions were improved using such combined images for mesh adaptation, especially for the square inclusion which has a long lateral interface difficult to resolve in axial strain alone. However, this is merely a proof-of-concept, because: (i) depending on boundary conditions, the axial-shear may not necessarily provide additional information, (ii) our image combination method of simple addition will not always effectively incorporate information from different modalities, and most importantly, (iii) axial-shear strain requires a separate excitation complicating the

acquisition procedure in a practical system.

XI. CONCLUSIONS

In this paper, a mesh adaptation approach has been proposed to improve the elasticity parameter reconstruction results obtained by solving the FEM inverse problem. Initialized by a regular triangular grid, mesh adaptation iteratively optimizes mesh connectivity and node positions in order to fit the mesh to an image. The use of axial strain imaging has been proposed for this purpose. Improvement over typical regular meshes has been demonstrated, after having applied the presented mesh adaptation approach. For mesh adaptation, intensity-wise combining axial and axial-shear strain images has also been shown, indicating further improvement in reconstructions. A study of the effect of noise on the reconstruction has showed that using adapted mesh, much higher noise can be tolerated in the reconstruction procedure. Experimental results from an breast phantom and an in-vivo breast study have been demonstrated, also exemplifying the use vibro-elastography images for mesh adaptation.

REFERENCES

- [1] K. Parker, S. Huang, R. Musulin, and R. Lerner, "Tissue response to mechanical vibrations for "sonoelasticity imaging"," *Ultrasound in Medicine and Biology*, vol. 16, no. 3, pp. 241–246, 1990.
- [2] J. Ophir, I. Céspedes, H. Ponnekanti, Y. Yazdi, and X. Li, "Elastography: a method for imaging the elasticity of biological tissues," *Ultrasonic Img*, vol. 13, no. 2, pp. 111–134, 1991.
- [3] A. P. Sarvazyan, O. V. Rudenko, S. D. Swanson, J. Fowlkes, and S. Y. Emelianov, "Shear wave elasticity imaging: a new ultrasonic technology of medical diagnostics," *Ultrasound in Medicine and Biology*, vol. 24, no. 9, pp. 1419–1435, 1998.
- [4] J. Bercoff, M. Tanter, and M. Fink, "Supersonic shear imaging: A new technique for soft tissue elasticity mapping," *IEEE Trans Ultrason Ferroelectr Freq Control*, vol. 51, no. 4, pp. 396–409, Apr 2004.
- [5] A. Manduca, R. Muthupillai, P. Rossman, J. Greenleaf, and R. Ehman, "Local wavelength estimation for magnetic resonance elastography," in *Proc Int Conf on Image Processing*, Sep 1996, pp. 527–530.
- [6] A. Manduca, T. Oliphant, M. Dresner, J. Mahowald, S. Kruse, E. Amromin, J. Felmler, J. Greenleaf, and R. Ehman, "Magnetic resonance elastography: Non-invasive mapping of tissue elasticity," *Medical Image Analysis*, vol. 5, pp. 237–254, 2001.
- [7] S. Papazoglou, U. Hamhaber, J. Braun, and I. Sack, "Algebraic Helmholtz inversion in planar magnetic resonance elastography," *Phys Med Biol*, vol. 53, no. 12, pp. 3147–3158, 2008.
- [8] K. R. Nightingale, M. L. Palmeri, R. W. Nightingale, and G. E. Trahey, "On the feasibility of remote palpation using acoustic radiation force," *J. Acoust. Soc. Am.*, vol. 110, no. 1, pp. 625–634, 2001.
- [9] E. Park and A. M. Maniatty, "Shear modulus reconstruction in dynamic elastography: time harmonic case," *Phys Med Biol*, vol. 51, pp. 3697–3721, 2006.
- [10] O. C. Zienkiewicz and R. L. Taylor, *The Finite Element Method*. Butterworth-Heinemann, 2000.
- [11] A. Arnold, S. Reichling, O. T. Bruhns, and J. Mosler, "Efficient computation of the elastography inverse problem by combining variational mesh adaption and a clustering technique," *Phys Med Biol*, vol. 55, pp. 2035–2056, 2010.
- [12] O. Goksel and S. E. Salcudean, "Image-based variational meshing," *IEEE Trans Med Imag*, vol. 30, no. 1, pp. 11–21, 2011.
- [13] F. Kallel and M. Bertrand, "Tissue elasticity reconstruction using linear perturbation method," *IEEE Trans Med Imag*, vol. 15, pp. 299–313, 1996.
- [14] M. Doyley, P. Meaney, and J. Bamber, "Evaluation of an iterative reconstruction method for quantitative elastography," *Phys Med Biol*, vol. 45, no. 6, pp. 1521–1540, 2000.
- [15] A. J. Romano, J. A. Bucaro, R. L. Ehnman, and J. J. Shirron, "Evaluation of a material parameter extraction algorithm using MRI-based displacement measurements," *IEEE Trans Ultrasonics, Ferroelectrics and Frequency Control*, vol. 47, no. 6, pp. 1575–1581, 2000.
- [16] E. E. Van Houten, M. I. Miga, J. B. Weaver, F. E. Kennedy, and K. D. Paulsen, "Three-dimensional subzone-based reconstruction algorithm for MR elastography," *Magn Reson Med*, vol. 45, no. 5, pp. 827–837, 2001.
- [17] M. I. Miga, "A new approach to elastography using mutual information and finite elements," *Phys Med Biol*, vol. 48, no. 4, pp. 467–480, 2003.
- [18] A. A. Oberai, N. H. Gokhale, M. M. Doyley, and J. C. Bamber, "Evaluation of the adjoint equation based algorithm for elasticity imaging," *Phys Med Biol*, vol. 49, no. 13, pp. 2955–2974, Jul 2004.
- [19] N. H. Gokhale, P. E. Barbone, and A. A. Oberai, "Solution of the nonlinear elasticity imaging inverse problem: the compressible case," *Inverse Problems*, vol. 24, no. 4, pp. 1–26, Aug 2008.
- [20] M. M. Doyley, "Model-based elastography: a survey of approaches to the inverse elasticity problem," *Physics in Medicine and Biology*, vol. 57, no. 3, pp. R35–73, 2012.
- [21] H. Eskandari, S. E. Salcudean, R. Rohling, and J. Ohayon, "Viscoelastic characterization of soft tissue from dynamic finite element models," *Phys Med Biol*, vol. 53, no. 22, pp. 6569–6590, 2008.
- [22] J. R. Shewchuk, "What is a good linear element? interpolation, conditioning, and quality measures," in *Int Meshing Roundtable*, 2002.
- [23] D. A. Field, "Qualitative measures for initial meshes," *Int J for Numerical Methods in Eng*, vol. 47, no. 4, pp. 887–906, 2000.
- [24] Q. Du and D. Wang, "Tetrahedral mesh generation and optimization based on centroidal voronoi tessellations," *Int J for Numerical Methods in Eng*, vol. 56, pp. 1355–1373, 2003.
- [25] L. Chen, "Mesh smoothing schemes based on optimal Delaunay triangulations," in *Int Meshing Roundtable*, 2004, pp. 109–120.
- [26] L. Chen and J. Xu, "Optimal Delaunay triangulation," *J Computational Mathematics*, vol. 22, no. 2, pp. 299–308, 2004.
- [27] P. Alliez, D. Cohen-Steiner, M. Yvinec, and M. Desbrun, "Variational tetrahedral meshing," *ACM Trans on Graphics (SIGGRAPH)*, vol. 24, no. 3, pp. 617–625, 2005.
- [28] T. Varghese and J. Ophir, "An analysis of elastographic contrast-to-noise ratio," *Ultrasound Med Biol*, vol. 24, pp. 915–924, 1998.
- [29] H. Eskandari, S. E. Salcudean, R. Rohling, and I. Bell, "Real-time solution of the finite element inverse problem of viscoelasticity," *Inverse Problems*, vol. 27, no. 8, pp. 085002+16, 2011.
- [30] R. Zahiri-Azar and S. Salcudean, "Motion estimation in ultrasound images using time domain cross correlation with prior estimates," *IEEE Trans Biomedical Eng*, vol. 53, no. 10, pp. 1990–2000, 2006.
- [31] X. Wen and S. E. Salcudean, "Power strain imaging based on vibro-elastography techniques," in *Proc. SPIE Med. Imag.*, 2007.
- [32] S. L. Floc'h, G. Cloutier, G. Finet, P. Tracqui, R. I. Pettigrew, and J. Ohayon, "On the potential of a new ivus elasticity modulus imaging approach for detecting vulnerable atherosclerotic coronary plaques: in vitro vessel phantom study," *Physics in Medicine and Biology*, vol. 55, no. 19, pp. 5701–21, 2010.
- [33] M. S. Richards and M. M. Doyley, "Investigating the impact of spatial priors on the performance of model-based ivus elastography," *Physics in Medicine and Biology*, vol. 56, no. 22, pp. 7223–46, 2011.
- [34] R. Azar, A. Baghani, S. Salcudean, and R. Rohling, "2-d high-frame-rate dynamic elastography using delay compensated and angularly compounded motion vectors: Preliminary results," *Ultrasonics, Ferroelectrics and Frequency Control, IEEE Transactions on*, vol. 57, no. 11, pp. 2421–36, 2010.
- [35] J. M. Abeysekera, R. Zahiri-Azar, O. Goksel, R. Rohling, and S. E. Salcudean, "Analysis of 2-d motion tracking in ultrasound with dual transducers," *Ultrasonics*, vol. 52, no. 1, pp. 156–168, 2012.
- [36] M. D. J. McGarry, E. E. W. V. Houten, P. R. P. nez, A. J. Pattison, J. B. Weaver, and K. D. Paulsen, "An octahedral shear strain-based measure of snr for 3d mr elastography," *Phys Med Biol*, vol. 56, no. 13, pp. N153–N164, 2011.
- [37] P. E. Barbone and N. H. Gokhale, "Elastic modulus imaging: on the uniqueness and nonuniqueness of the elastography inverse problem in two dimensions," *Inverse Problems*, vol. 20, no. 1, p. 283, 2004.